Temperature-induced Displacement of Supertall Structures: a Case Study

Yi-ding Hu[1,2], Rongrong Hou[2], Qi Xia[2*], Yong Xia[2]

1 School of Information Engineering, Wuyi University, Jiangmen, China

2 Department of Civil and Environmental Engineering, The Hong Kong Polytechnic University, Hong Kong, China

* Corresponding author, Email: q.xia@polyu.edu.hk

Abstract

For a supertall structure, the temperature effect is an important factor that must be considered during the design, construction, and performance assessment. In this article, temperature-induced displacement of the 600-meter-high Canton Tower is studied by the data-driven approach based on the sufficient real measurement data obtained from the structural health monitoring system. A multiple linear regression model is employed to establish the quantitative relation between the displacement and temperature data at different facades and sections of the structure in different seasons. Results show that an ordinary linear regression (OLR) model is able to fit the monitoring data well. However, the model fails to interpret the physical meaning of the model coefficients. A regularized linear regression (RLR) model is then employed and validated to describe the temperature-induced displacement of the structure. The physical relationship between the temperature and displacement is provided. Finally, the model is also used to separate the temperature- and wind-induced displacement of the supertall structure.

Keywords: temperature, supertall structure, linear regression, regularization

Introduction

During the service periods of the infrastructure, temperature variations in the structural components induced by daily, seasonal, and yearly will cause negligible thermal stress and deformations (Peeters, et al., 2001; Xia, et al., 2012; Zhou, et al., 2017; Hu, et al., 2017; Xia, et al., 2017; Tian, et al., 2017). In high-rise buildings, significant temperature differences may occur between the exterior and adjacent interior columns, and any restraint to their relative deformations will induce stresses in the members concerned. At heights above 20 stories this temperature effect may be significant, and it becomes desirable to investigate the influence of the thermal deformations on the structural actions (Smith and Coull, 1991). For a supertall structure, the temperature-induced daily movement may be similar to or even larger than the typhoon-induced motion (Xia et al., 2014). Therefore, it is of great importance to investigate temperature effects on supertall structures especially.

The temperature effects on tall buildings have been studied for decades. Since 1993, a long-term monitoring about the change of dynamic responses and structural properties for Republic Plaza, a 280-m office tower, was conducted by Brownjohn and colleagues (Brownjohn, 2005). The total movements of this building were estimated to be of the order of 0.1 m, which were induced by wind and temperature together. Even after ten years of monitoring, the deflections of the building due to temperature were not determined (Brownjohn and Pan, 2008). Pirner and Fischer (1999) carried out long-term observations of stresses and temperature of a 198-m-high TV tower and revealed that the stresses due to temperature changes were nonuniform

along the circumference of the cylinder and not negligible. Tamura et al. (2002) used the Real Time Kinematic GPS (RTK-GPS) system and found that the maximum deformation of a 108-m-high steel tower top on a calm and fine weather day was about 4 cm. Seco et al. (2007) monitored a 30-m-tall concrete building continuously and analyzed the correlation between the observed displacements and the weather variables such as temperature, direct solar radiation and wind, but failed to establish the correlation between the displacements and the weather variables statistically due to the small value of the displacements observed in this building. Nayeri et al. (2008) investigated the effects of environmental and operational conditions on the estimated dynamic properties of a 17-story steel frame building located on the UCLA campus and found that there is a strong correlation between the modal frequency variations and the temperature variations in a 24 h period. Breuer et al. (2008, 2010) employed the RTK-GPS to investigate the displacement of the Stuttgart TV Tower (212 m high) caused by the combined influence of solar radiation and daily air temperature variation during different seasons and conditions. Pehlivan et al. (2015) also used the RTK-GPS to measure the displacement of the 220-m-high Endem TV tower over a period of 9 days. The monitoring results showed that the tower experienced a half-ecliptic movement due to the solar radiation and varying air temperature. These studies focused on air or ambient temperature but not structural temperature. Although the two sets of temperature are correlated, the structural responses (displacement and stress) directly depend on the temperature of structural components. For this reason, the above studies could not obtain the quantitative relation between

the responses and temperature.

It was until recently that a few studies combined finite element (FE) model analysis and field monitoring data to quantify the temperature effects on supertall structures. Ni et al. (2011) developed monitoring-based temperature distribution models of Guangzhou Tower in order to serve as a reliable input for numerical simulation of the temperature-induced deformations. Su et al. (2017a) inputted the structural temperature of the 600-m tall Canton Tower into an FE model of the global structure and calculated the temperature-induced deformation. They then used the model to separate the typhoon-induced quasi-static responses from the measured displacement (Su et al., 2017b). The approach of FE model could handle complex temperature loading of the structure, but these methods usually need temperature distribution of the whole structure and manual intervention. Therefore, the calculation is time-consuming and online evaluation is thus very difficult. Moreover, the temperature data of all nodes of the FE model are not available and some assumptions are required in FE analysis. Consequently, the temperature-induced responses calculated from the FE analysis may have non-unique solution and be not accurate.

Based on a large amount of structural temperature and displacement data provided by the more refined structural health monitoring (SHM) system, the more accurate quantitative analysis of temperature-induced displacement can be obtained directly by data-driven methods, including machine learning, signal analysis, and statistical analysis. Data-driven methods make it feasible for fast and efficient calculation and avoid the error resulted from the inaccuracy of the FE model, thereby

overcome the disadvantages of the FE model methods mentioned above. For super tall structures, data-driven quantitative analysis of temperature-induced displacement was not investigated yet.

This article proposes a data-driven method to study temperature effects on the Canton Tower. Appropriate structural temperature and displacement data sets are selected from huge amount of records measured by the SHM system of the tower and be cleaned subsequently. Then, the multiple linear regression analysis is conducted to reveal the quantitative relation between the monitoring temperature and displacement data. Ordinary linear regression (OLR) and regularized linear regression (RLR) models are compared in terms of the physical interpretation and prediction ability. Finally, the proposed scheme is used to decompose wind-induced displacement from the total measured responses under the monsoon circumstance.

Canton Tower and its monitoring system

The Canton Tower, located in Guangzhou City, is a concrete–steel composite structure that consists of a 454-m-high main tower and a 146-m-high antennary mast. The main tower comprises a reinforced concrete inner tube and a steel outer tube of concrete-filled-tube (CFT) columns. It contains 36 floors and four levels of connection girders that join the inner tube to the outer tube, as shown in Figure 1.

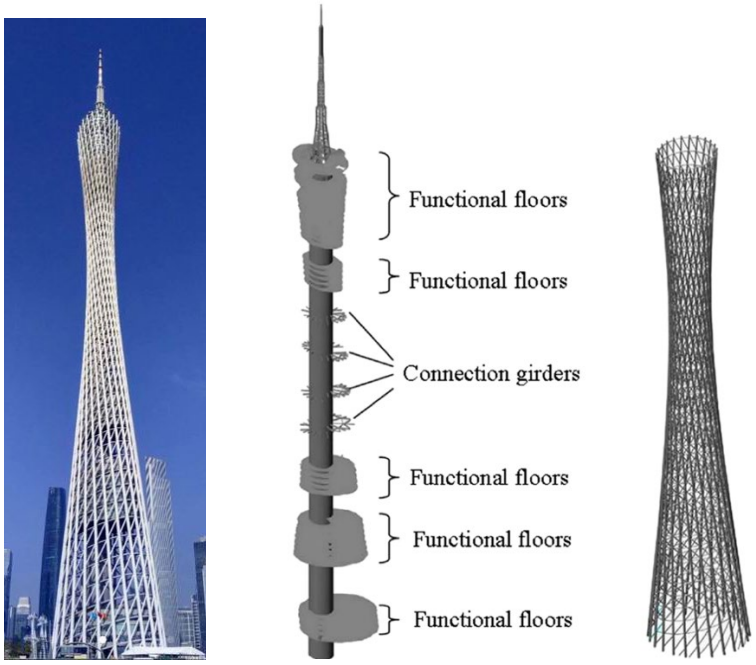

(a) Perspective view (b) Inner tube (c) Outer tube

Figure 1. The structural configuration of Canton Tower

A sophisticated SHM system consisting of 16 different types of over 700 sensors has been designed and installed by the consortium of Hong Kong Polytechnic University and Sun Yat-Sen University (Ni et al., 2009). The temperature and strain monitoring subsystems are distributed along 12 sections at different heights of the structure, that is, 32.8 m, 100.4 m, 121.2 m, 173.2 m, 204.4 m, 230.4 m, 272.0 m, 303.2 m, 334.4 m, 355.2 m, 376.0 m, and 433.2 m, as shown in Figure 2. Sections 5–8 correspond to the four levels of the connection girders. The data on each section are collected by the corresponding substations and then transmitted to a central control room.

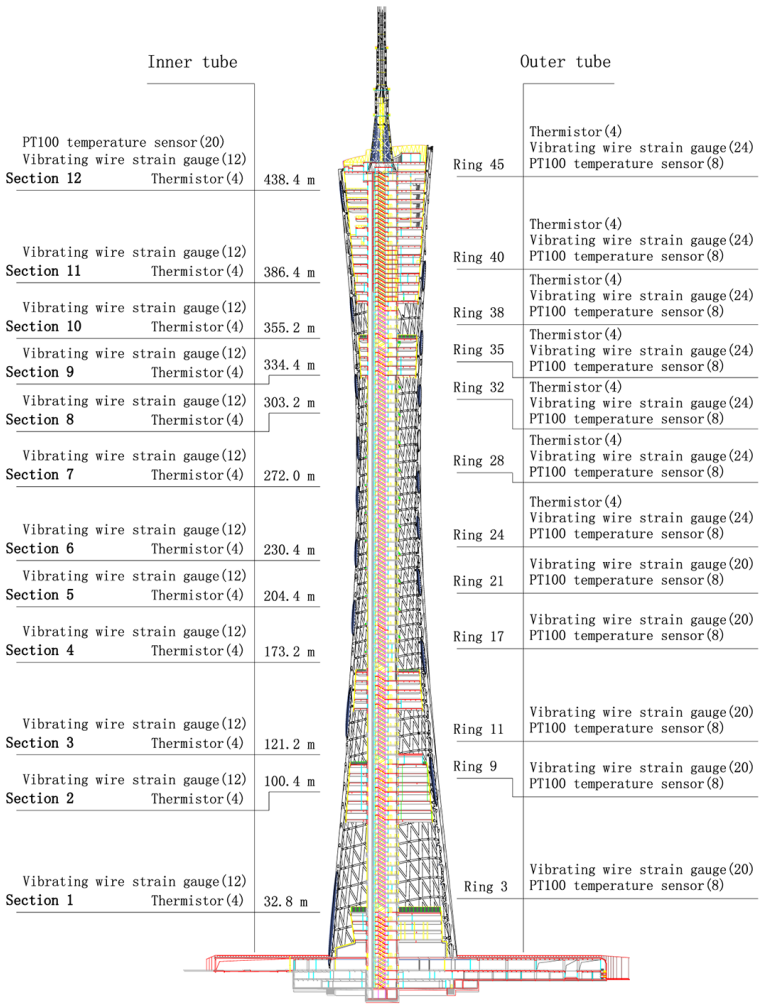

Figure 2. Sections of the temperature and strain monitoring system

Figures 3(a) and 3(b) show the plan view of Section 3 and 8 and their temperature monitoring points, which represent the sections with and without functional floors, respectively. The inner tube has an oval shape with a constant dimension of 14 m × 17 m. The long axis of the inner tube is directed toward of 18° west to north. The outer tube consists of 24 CFT columns, uniformly spaced in an oval while being inclined in the vertical direction. The CFT columns are interconnected transversely by steel ring beams and bracings. The dimension of the oval decreases from 50 m × 80 m at the underground level to a minimum of 20.65 m × 27.5 m at the height of 280 m and then

increases to 40.5 m × 54 m at the top of the main tower. At each of points 1 to 4 on the monitoring sections of the inner tube, one thermistor was embedded in the middle of concrete core wall. Point A ~ D at each section of the outer tube were installed with temperature sensors. Each CFT column has two PT100 temperature sensors attached on the steel surface, one facing to the inner tube and the other to outward, as shown in Figure 3(c). Moreover, on Section 8, one thermistor was embedded inside the concrete of each CFT column, which was located at one-third of the radius from the column surface. It is noted the plane locations of Points A to D vary as the height of the CFT columns increases due to the tower's twisted shape.

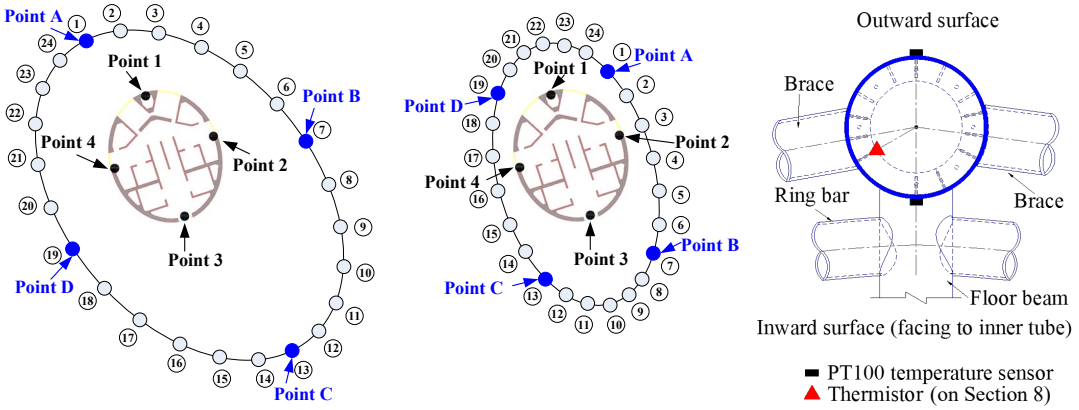

(a) Section 3 (b) Section 8 (c) Plan view of CFT

Figure 3. The temperature monitoring points of typical sections

A GPS system was installed at the top of Canton Tower to monitor displacement. The reference station installed 3 m above the platform at 10.2 m and the rover station on a chimney at approximately 6 m above the sightseeing platform at 459.2 m. The sampling rate of the GPS was set to 1 Hz. The collected GPS data have been

transferred to the horizontal displacement in the east-west and north-south directions.

The climate of Guangzhou City is the typical subtropical monsoon marine climate, which has hot summers and warm winters. The average annual sunshine duration is about 1688.9 h. The air temperature is from about 2 to 38.7°C and the annual mean temperature is about 22.8°C (Chen et al., 2012). Therefore, it is of great importance to study the temperature-induced displacement of the complex tower structure under such climate conditions. The measured GPS displacement and temperature data in the year of 2013 are used to investigate the thermal performance of the tower.

Data preprocessing

Data selection

In order to quantify the relation between the displacement and temperature, the data collected at wind speed less than 3.3 m/s (which is defined as light breeze according to Beaufort wind force scale) are chosen to minimize the influence of the wind load. In addition, the data on sunny days in different seasons are selected so that the temperature range covers as widely as possible. Considering the above factors and the data completeness of all measurement points, four data segments are selected in 2013 for model training. The first data segment was from 15:00:01 on April 12 to 15:00:00 on April 14, including 48 hours; the second from 00:00:01 on June 15 to 00:00:00 on June 19, including 96 hours; the third from 00:00:01 on November 6 to 00:00:00 on November 10, including 96 hours, and the fourth from 00:00:01 on December 1 to

06:00:00 on December 4, including 78 hours. All time instants here are Hong Kong Time.

The temperature data of Sections 3 and 8 are selected because they represent levels with and without functional floors, respectively. Su et al. (2017a) showed that the temperature measured by the thermistors inside the CFT columns could be considered the effective temperature of the composite section of the column. In Section 3, the averaged temperature of the inward and outward surfaces of the CFT columns is used as no thermistor was installed inside the CFT columns in the Section. In conclusion, sixteen temperature measurement points on the two sections are chosen: T_{31}, T_{32}, T_{33} and T_{34} refer to the temperature data of the four inner tube measurement points on Section 3; T_{3A}, T_{3B}, T_{3C} and T_{3D} represent the averaged temperature data of the CFT columns on Section 3; T_{81}, T_{82}, T_{83} and T_{84} are those of the four inner tube measurement points on Section 8; and T_{8A}, T_{8B}, T_{8C} and T_{8D} represent the effective temperature data of the CFT columns on Section 8.

Data cleaning

During the data acquisition, out-of-range data or corrupted data may occur due to various reasons such as sensor failures or software errors. Therefore, the raw data have to be cleaned, such as filling missing values, smoothing noisy data, and removing outliers. The process can be time-consuming and tedious but cannot be ignored. In this paper, temperature and displacement data are cleaned before the regression analysis.

Temperature data cleaning

The sampling rate of all temperature sensors is one record per minute. The temperature data were missed only one or two records per day, and duplicated one record very occasionally. The temperature data are cleaned as follows: (i) All the duplicated records are eliminated. (ii) Since temperature of the structure does not change drastically within one or two minutes, the missed or eliminated data are added through linear interpolation. (iii) Temperature data are averaged every 10 minutes in order to remove random fluctuations. As an example, Figures 4(a) and (b) show the averaged temperature time histories of the 16 points at Sections 3 and 8 from 00:00:01 on November 6, 2013 to 00:00:00 on November 10, 2013. In Figure 4(a), the outer tube columns have larger temperature variations than the inner tube points. This is because Section 3 has a functional floor that is enclosed by a curtain wall. Consequently the inner tube inside the curtain wall has a relatively stable temperature variation and the outer tube outside the curtain wall has a relatively larger temperature variation. Section 8, however, has no such functional floor and thus the inner tube and outer tube have similar temperature variation trend, as shown in Figure 4(b). Moreover, different facades arrived the maximum temperature at different time in the day.

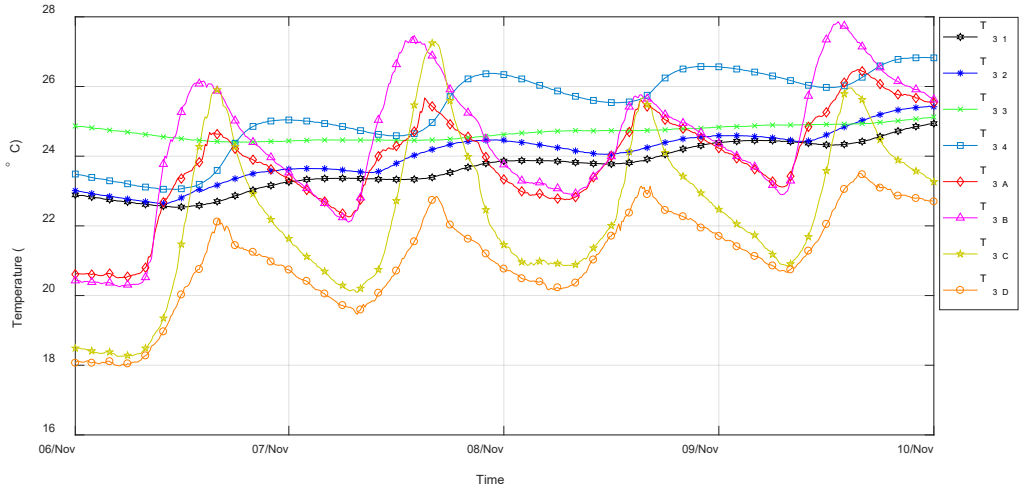

(a) Section 3

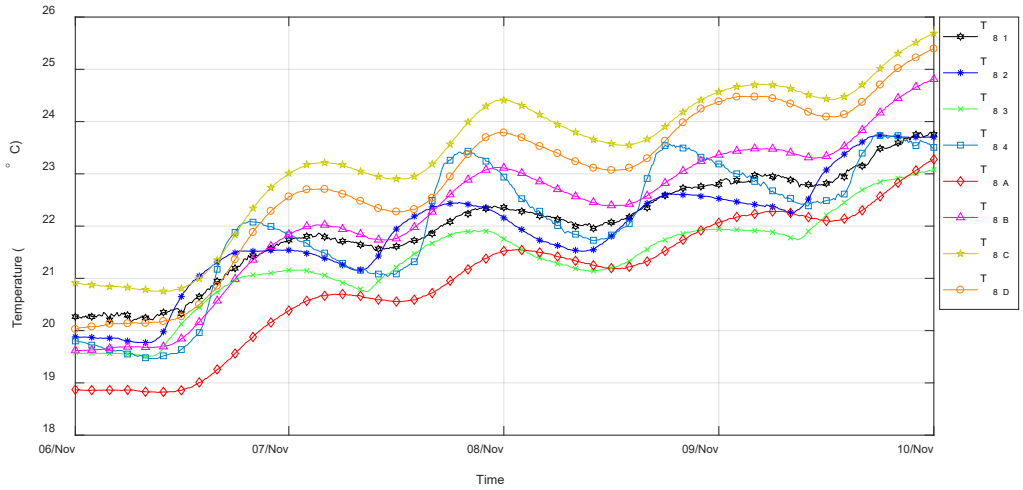

(b) Section 8

Figure 4. Temperature data of Sections 3 and 8

GPS data cleaning

The displacement time histories recorded by GPS were lost or drifted occasionally. These phenomena may occur when the number of visible satellites decreases suddenly (Chan and Xu, 2008). Figure 5(a) displays the measured raw displacement of the tower top in the east-west direction on Nov. 6, 2013. Abrupt changes occurred at some time instances. These abnormal data should be removed to reduce the interference in the

229 analysis and the cleaned data are shown in Figure 5(b). Same as the temperature data,
230 the missed or eliminated displacement data are added through linear interpolation, and
231 then averaged every 10 minutes to eliminate the random errors and small vibrations due
232 to wind or ambient excitations. The averaged displacement is shown in Figure 5(c). It is
233 noted that only quasi-static response of the tower due to temperature are taken into
234 consideration.

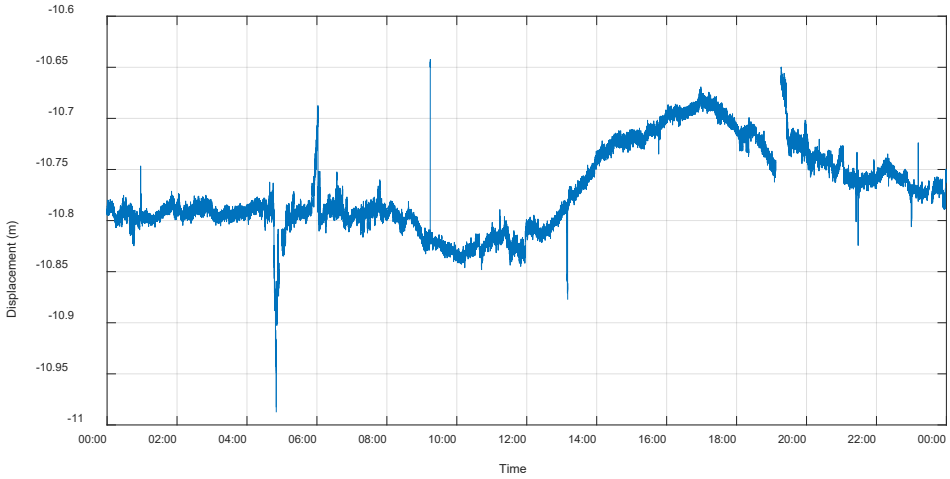

235

236 (a) Raw data

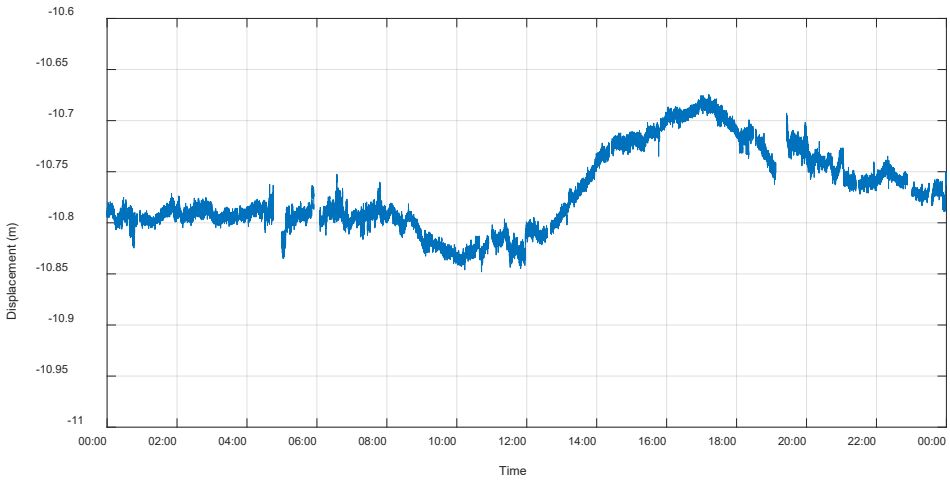

237

238 (b) Processed data

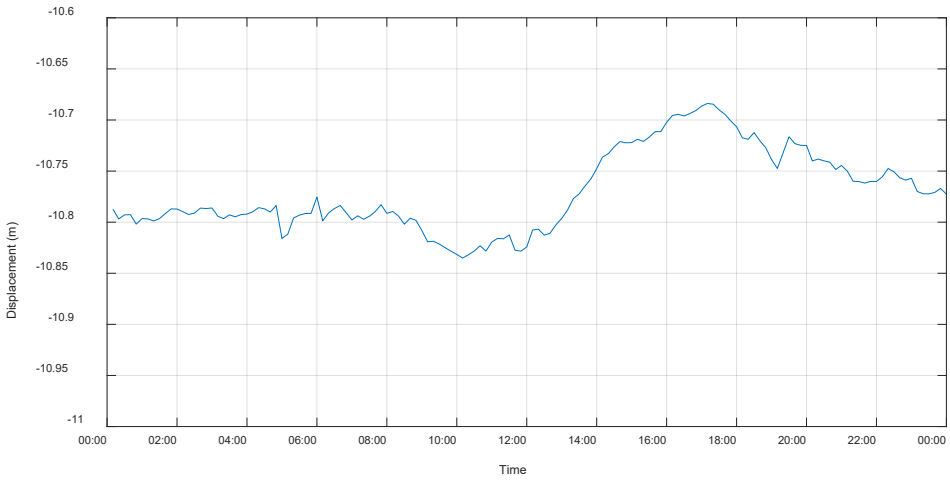

(c) Data averaged over 10 minutes

Figure 5. Displacement of the tower top in east-west direction on Nov. 6, 2013

Linear Regression analysis

Ordinary linear regression (OLR)

Since temperature has a linear effect on the structural responses, the relation between the tower top displacement and structural temperature can be represented by the following linear regression equation

$$y_i = \beta_0 + \beta_1 x_{i1} + \beta_1 x_{i2} + \cdots + \beta_p x_{ip} + \varepsilon_i \quad (i = 1,2,\cdots,n) \tag{1}$$

where y_i is the measured displacement at *i*th time step, x_{ij} $(j = 1,2,\cdots,p)$ is the *i*th temperature data measured at location *j*, β_j $(j = 0,1,\cdots,p)$ is the coefficient, and ε_i is the *i*th random error. The least squared solution of $\hat{\beta}$ is obtained by minimizing the following objective function

$$J(\hat{\beta}) = \sum_{i=1}^{n} \left(y_i - \hat{\beta}_0 - \sum_{j=1}^{p} x_{ij} \hat{\beta}_j \right)^2 \tag{2}$$

Eq. (1) can be written in the matrix form:

$$Y = \mathbf{X}\boldsymbol{\beta} + \boldsymbol{\varepsilon} \tag{3}$$

where

$$Y = \begin{bmatrix} y_1 \\ \vdots \\ y_n \end{bmatrix} \quad \mathbf{X} = \begin{bmatrix} 1 & x_{11} & \cdots & x_{1p} \\ \vdots & \vdots & \vdots & \vdots \\ 1 & x_{n1} & \cdots & x_{np} \end{bmatrix} \quad \boldsymbol{\beta} = \begin{bmatrix} \beta_0 \\ \vdots \\ \beta_p \end{bmatrix} \quad \boldsymbol{\varepsilon} = \begin{bmatrix} \varepsilon_1 \\ \vdots \\ \varepsilon_n \end{bmatrix} \tag{4}$$

$Y \in \mathbb{R}^n$, $\mathbf{X} \in \mathbb{R}^{n\times(p+1)}$, $\boldsymbol{\beta} \in \mathbb{R}^{p+1}$ and $\boldsymbol{\varepsilon} \in \mathbb{R}^n$.

The objective function Eq. (2) can also be written as

$$J(\hat{\beta}) = \left\| Y - \mathbf{X}\widehat{\boldsymbol{\beta}} \right\|_2^2 \tag{5}$$

and the least squared solution is given as

$$\widehat{\boldsymbol{\beta}} = (\mathbf{X}^{\mathrm{T}}\mathbf{X})^{-1}\mathbf{X}^{\mathrm{T}}Y \tag{6}$$

where superscript "T" indicates the transpose of the matrix, then the estimated response is

$$\hat{Y} = \mathbf{X}\widehat{\boldsymbol{\beta}} \tag{7}$$

The above OLR analysis is applied to the east-west or north-south displacement of the tower and temperature data at 16 points. Figures 6(a) and (b) show the measured and fitted displacement in the selected four data segments. The daily horizontal displacement of the tower in winter is larger than that in summer. This is because the temperature variation of the tower in winter is more significant than in summer in Guangzhou city. Moreover, the horizontal displacement in summer mainly occurred in the east-west direction, which is because Guangzhou is located on the Tropic of Cancer and the sun moves from the east to the west in the daytime. In the winter season, the sun moves to the Southern Hemisphere and the temperature difference between the south and north facades of the tower is significant. Consequently, the tower displacement in the south-north direction is significant. The above scenarios are observed in other years (Su et al., 2017a).

The root mean square error (RMSE) of the fitting curves of whole east-west direction displacement is calculated as 8.63 mm, and that of north-south direction is 8.18 mm. The correlation coefficient of the OLR analysis is 0.9723 and 0.9915 for the east-west and north-south displacement, respectively. Therefore, the OLR model fits the measured data very well. The local discrepancy may be due to two reasons. One is the measurement noise, particularly the GPS data, which is assumed in the millimeter to centimeter level. The other factor is the displacement due to other loadings such as winds, although small.

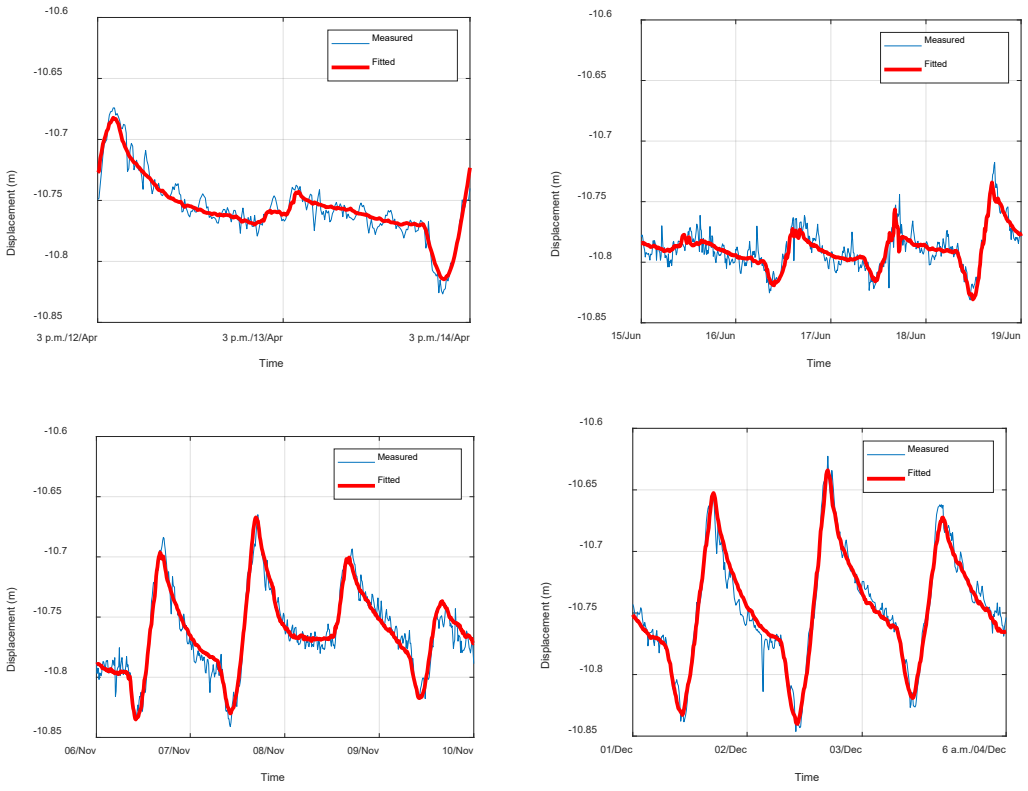

(a) East-west direction

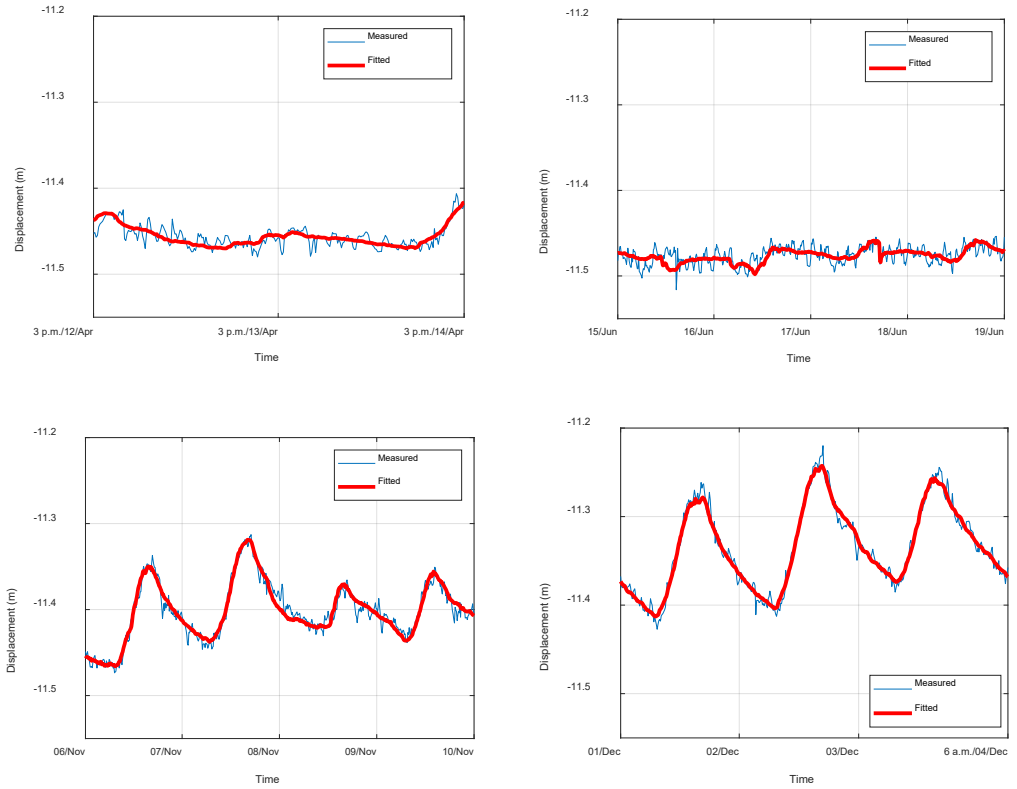

(b) North-south direction

Figure 6. The measured and fitted horizontal displacement of the tower top by OLR

The corresponding coefficients of the linear regression model are listed in Table 1, in which $\hat{\beta}_0$ is the constant term, $\hat{\beta}_1 \sim \hat{\beta}_4$ are coefficients corresponding to inner tube temperature of points 1 ~ 4 of Section 3, $\hat{\beta}_5 \sim \hat{\beta}_8$ corresponding to average temperature of outer tube points A ~ D of Section 3, $\hat{\beta}_9 \sim \hat{\beta}_{12}$ inner tube temperature of points 1 ~ 4 of Section 8, and $\hat{\beta}_{13} \sim \hat{\beta}_{16}$ outer tube temperature of points A~ D of Section 8. Superscripts "EW" and "NS" represent the east-west and north-south displacement, respectively. The physical meaning of $\hat{\beta}_1 \sim \hat{\beta}_{16}$ indicates the effect of the temperature data at the particular point on the horizontal displacement of the tower top. Take Section 8 as an example (refer to Figure 3 (b)). A temperature increase at

point 1 in the inner tube and points A and D in the outer tube will cause the tower top lean to the south, which is defined as negative horizontal displacement in the north-south direction. Consequently coefficients $\hat{\beta}_9^{NS}$, $\hat{\beta}_{13}^{NS}$ and $\hat{\beta}_{16}^{NS}$ should be negative. In contrast, $\hat{\beta}_{11}^{NS}$, $\hat{\beta}_{14}^{NS}$ and $\hat{\beta}_{15}^{NS}$ should be positive. The signs of $\hat{\beta}_{10}^{NS}$ and $\hat{\beta}_{12}^{NS}$ are hard to determine because points 2 and 4 are located near to the central line of the tower. However, the estimated coefficients $\hat{\beta}_{13}^{NS}$ and $\hat{\beta}_{14}^{NS}$ are incorrect. The main reason may be that the temperature data of the 4 columns in the outer tube have a similar trend, which causes the matrix $\mathbf{X^T X}$ ill-posed. Consequently, the measurement noise leads to the significant errors in the estimation of the coefficients. To avoid the ill-posedness, the regularized regression will be employed in the next section.

Table 1. Coefficients of the OLR regression model

Position associated with the coefficient			East-west direction		North-south direction	
Constant term			$\hat{\beta}_0^{EW}$	− 10.79859	$\hat{\beta}_0^{NS}$	− 11.47543
Section 3	Inner tube	Point 1	$\hat{\beta}_1^{EW}$	− 0.01228	$\hat{\beta}_1^{NS}$	0.00277
		Point 2	$\hat{\beta}_2^{EW}$	0.03689	$\hat{\beta}_2^{NS}$	0.01035
		Point 3	$\hat{\beta}_3^{EW}$	− 0.00777	$\hat{\beta}_3^{NS}$	− 0.01794
		Point 4	$\hat{\beta}_4^{EW}$	− 0.00082	$\hat{\beta}_4^{NS}$	0.00961
	Outer tube	Point A	$\hat{\beta}_5^{EW}$	− 0.00964	$\hat{\beta}_5^{NS}$	− 0.00794
		Point B	$\hat{\beta}_6^{EW}$	− 0.01185	$\hat{\beta}_6^{NS}$	0.01150
		Point C	$\hat{\beta}_7^{EW}$	0.02180	$\hat{\beta}_7^{NS}$	0.01521
		Point D	$\hat{\beta}_8^{EW}$	0.00760	$\hat{\beta}_8^{NS}$	− 0.00830
Section 8	Inner tube	Point 1	$\hat{\beta}_9^{EW}$	− 0.01007	$\hat{\beta}_9^{NS}$	− 0.02053
		Point 2	$\hat{\beta}_{10}^{EW}$	− 0.02391	$\hat{\beta}_{10}^{NS}$	− 0.01929
		Point 3	$\hat{\beta}_{11}^{EW}$	− 0.00578	$\hat{\beta}_{11}^{NS}$	0.02390
		Point 4	$\hat{\beta}_{12}^{EW}$	0.02179	$\hat{\beta}_{12}^{NS}$	0.00555
	Outer tube	Point A	$\hat{\beta}_{13}^{EW}$	0.00255	$\hat{\beta}_{13}^{NS}$	0.00658
		Point B	$\hat{\beta}_{14}^{EW}$	0.00799	$\hat{\beta}_{14}^{NS}$	− 0.01125
		Point C	$\hat{\beta}_{15}^{EW}$	− 0.02339	$\hat{\beta}_{15}^{NS}$	0.01256
		Point D	$\hat{\beta}_{16}^{EW}$	0.00997	$\hat{\beta}_{16}^{NS}$	− 0.01032

Regularized linear regression (RLR)

In the RLR analysis, a regularization term is added into the objective function Eq. (2) as follows (Hastie et al. 2009)

$$J(\hat{\beta}) = \sum_{i=1}^{n}\left(y_i - \hat{\beta}_0 - \sum_{j=1}^{p} x_{ij}\hat{\beta}_j \right)^2 + k\sum_{j=1}^{p}\hat{\beta}_j^2 \tag{8}$$

where k $(k \geq 0)$ is the regularization parameter that controls the trade-off between the first item (referred to as the residual norm) and the second item (solution norm).

Notice that the constant term $\hat{\beta}_0$ has been left out of the penalty term, because it would make the results depend on the origin chosen for Y (Hastie et al. 2009). Therefore, the solution procedure of Eq. (8) is recommended by two steps.

The first step is to get the solution $\hat{\beta}_j'(j = 1,2,\cdots,p)$, which is computed by replacing x_{ij} with the standardization $z_{ij} = (x_{ij} - \bar{x}_j)/\sigma_{x_j}$, and replacing y_i with $y_i - \bar{y}$, where $\bar{x}_j$ and $\bar{y}$ are mean values and σ_{x_j} is the standard deviation. Eq. (8) can be re-written as the matrix form:

$$J(\widehat{\boldsymbol{\beta}}') = \left\|Y' - \mathbf{Z}\widehat{\boldsymbol{\beta}}'\right\|_2^2 + k\left\|\widehat{\boldsymbol{\beta}}'\right\|_2^2 \tag{9}$$

The least squares solution of Eq. (9) is

$$\widehat{\boldsymbol{\beta}}' = (\mathbf{Z}^{\mathrm{T}}\mathbf{Z} + k\mathbf{I})^{-1}\mathbf{Z}^{\mathrm{T}}Y' \tag{10}$$

where $Y' = \begin{bmatrix} y_1 - \bar{y} \\ \vdots \\ y_n - \bar{y} \end{bmatrix}$, $\mathbf{Z} = \begin{bmatrix} z_{11} & z_{12} & \cdots & z_{1p} \\ \vdots & \vdots & \vdots & \vdots \\ z_{n1} & z_{n2} & \cdots & z_{np} \end{bmatrix}$, $\widehat{\boldsymbol{\beta}}' = \begin{bmatrix} \hat{\beta}_1' \\ \vdots \\ \hat{\beta}_p' \end{bmatrix}$. $\mathbf{I}$ is the identity matrix, and $\mathbf{I} \in \mathbb{R}^{p\times p}$, $Y' \in \mathbb{R}^n$, $\mathbf{Z} \in \mathbb{R}^{n\times p}$ and $\widehat{\boldsymbol{\beta}}' \in \mathbb{R}^p$.

The coefficients $\widehat{\boldsymbol{\beta}}'$ are estimated from Eq. (10) without the constant term. The coefficients of Eq. (8), $\hat{\beta}_j$ $(j = 1,2,\cdots,p)$ can then be calculated by

$$\hat{\beta}_j = \hat{\beta}_j'/\sigma_{x_j}, (j = 1,2,\cdots,p) \tag{11}$$

337 The second step is to infer $\hat{\beta}_0$ by

338 $$\hat{\beta}_0 = \overline{y} - \sum_{j=1}^{p} \overline{x}_j \hat{\beta}_j \quad (12)$$

339 In Eq. (9), an appropriate regularization parameter k is usually selected through
340 the L-curve method, which shows that the plot of the residual norm $\left\|Y' - \mathbf{Z}\hat{\beta}'\right\|_2$
341 against the solution norm $\left\|\hat{\beta}'\right\|_2$ resembles an "L" shape (Hansen and O'Leary,
342 1993). The residual norm represents the degree of fitting while the solution norm
343 represents the smoothness of the solution. The RLR analysis is applied to the present
344 study. The residual norm versus the solution norm is plotted in Figure 7 for k
345 ranging from 0 to 300. When $k = 0$, the RLR analysis is the same as the OLR
346 analysis. For a small k, the residual term dominates the objective function (Eq. (9))
347 and thus the solution term is larger to reduce the overall misfit. For a larger
348 regularization parameter, the solution term will dominate the objective function and
349 thus be penalized more. As a result, the solution norm tends to decrease and the
350 residual norm increases. Hansen and O'Leary (1993) suggested to choose the
351 regularization parameter that corresponds to the point of the maximum curvature of
352 the L-curve, or close to the corner of the "L" curve. In this study, the value of k
353 corresponding to the maximum curvature of the L-curve was $k = 2.8$ for the
354 east-west direction and $k = 2.2$ for the north-south direction.
355

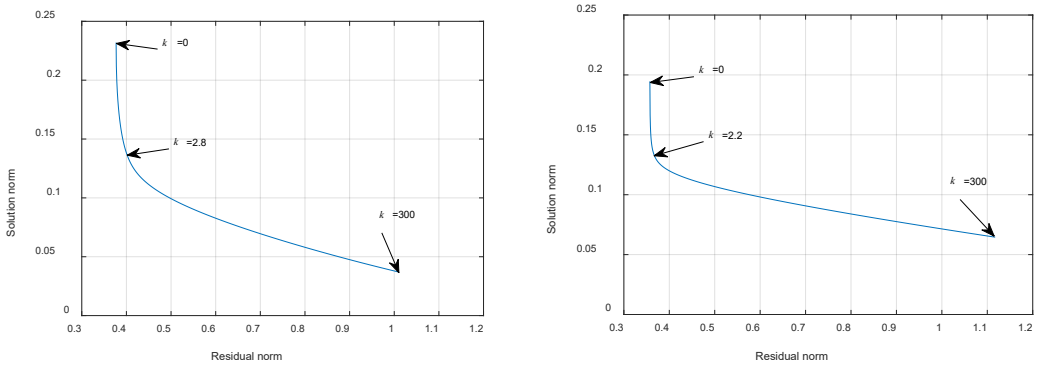

(a) East-west direction (b) North-south direction

Figure 7. L-curve for different regularization parameter k

When the optimal k is selected, the coefficients of the regression model are calculated by Eq. (11) and Eq. (12), and listed in Table 2. In particular for Section 8, $\hat{\beta}_9^{NS}$, $\hat{\beta}_{13}^{NS}$, $\hat{\beta}_{16}^{NS}$, $\hat{\beta}_{10}^{EW}$ and $\hat{\beta}_{14}^{EW}$ are negative, and $\hat{\beta}_{11}^{NS}$, $\hat{\beta}_{14}^{NS}$, $\hat{\beta}_{15}^{NS}$, $\hat{\beta}_{12}^{EW}$ and $\hat{\beta}_{16}^{EW}$ are positive. All are consistent with the qualitative analysis of the physical meaning of the coefficients. For example, the absolute value of the coefficient of the outer tube is generally larger than that of the inner tube on the Section 3. The physical meaning corresponds to the temperature variations of out tube are greater than the inner cylinder's. This phenomenon is consistent with Figure 4. Therefore, the RLR model is validated. Figure 8 shows the fitting results using the RLR analysis. The RMSE of the fitting curves is 9.19 mm for the east-west direction displacement, and 8.36 mm for the north-south direction. Both errors are slightly larger than those using the OLR analysis. This is reasonable because the OLR approach is equivalent to $k = 0$ in the RLR approach. As shown in Figure 7, the residue for $k = 0$ is less than those of $k = 2.8$ (East-west direction) or $k = 2.2$ (North-south direction).

Table 2. Coefficients of the RLR model

Position associated with the coefficient			East-west direction		North-south direction	
Constant term			$\hat{\beta}_0^{EW}$	− 10.75768	$\hat{\beta}_0^{NS}$	− 11.45632
Section 3	Inner tube	Point 1	$\hat{\beta}_1^{EW}$	−0.00102	$\hat{\beta}_1^{NS}$	− 0.00386
		Point 2	$\hat{\beta}_2^{EW}$	0.00669	$\hat{\beta}_2^{NS}$	0.00362
		Point 3	$\hat{\beta}_3^{EW}$	− 0.00644	$\hat{\beta}_3^{NS}$	− 0.01073
		Point 4	$\hat{\beta}_4^{EW}$	0.00005	$\hat{\beta}_4^{NS}$	0.00892
	Outer tube	Point A	$\hat{\beta}_5^{EW}$	− 0.01046	$\hat{\beta}_5^{NS}$	− 0.00871
		Point B	$\hat{\beta}_6^{EW}$	− 0.01295	$\hat{\beta}_6^{NS}$	0.01219
		Point C	$\hat{\beta}_7^{EW}$	0.02419	$\hat{\beta}_7^{NS}$	0.01606
		Point D	$\hat{\beta}_8^{EW}$	0.00547	$\hat{\beta}_8^{NS}$	− 0.01189
Section 8	Inner tube	Point 1	$\hat{\beta}_9^{EW}$	− 0.00350	$\hat{\beta}_9^{NS}$	− 0.00951
		Point 2	$\hat{\beta}_{10}^{EW}$	− 0.01087	$\hat{\beta}_{10}^{NS}$	− 0.00973
		Point 3	$\hat{\beta}_{11}^{EW}$	− 0.00490	$\hat{\beta}_{11}^{NS}$	0.00695
		Point 4	$\hat{\beta}_{12}^{EW}$	0.01835	$\hat{\beta}_{12}^{NS}$	0.00712
	Outer tube	Point A	$\hat{\beta}_{13}^{EW}$	− 0.00127	$\hat{\beta}_{13}^{NS}$	− 0.00211
		Point B	$\hat{\beta}_{14}^{EW}$	− 0.00018	$\hat{\beta}_{14}^{NS}$	0.00556
		Point C	$\hat{\beta}_{15}^{EW}$	− 0.00656	$\hat{\beta}_{15}^{NS}$	0.00827
		Point D	$\hat{\beta}_{16}^{EW}$	0.00547	$\hat{\beta}_{16}^{NS}$	− 0.01115

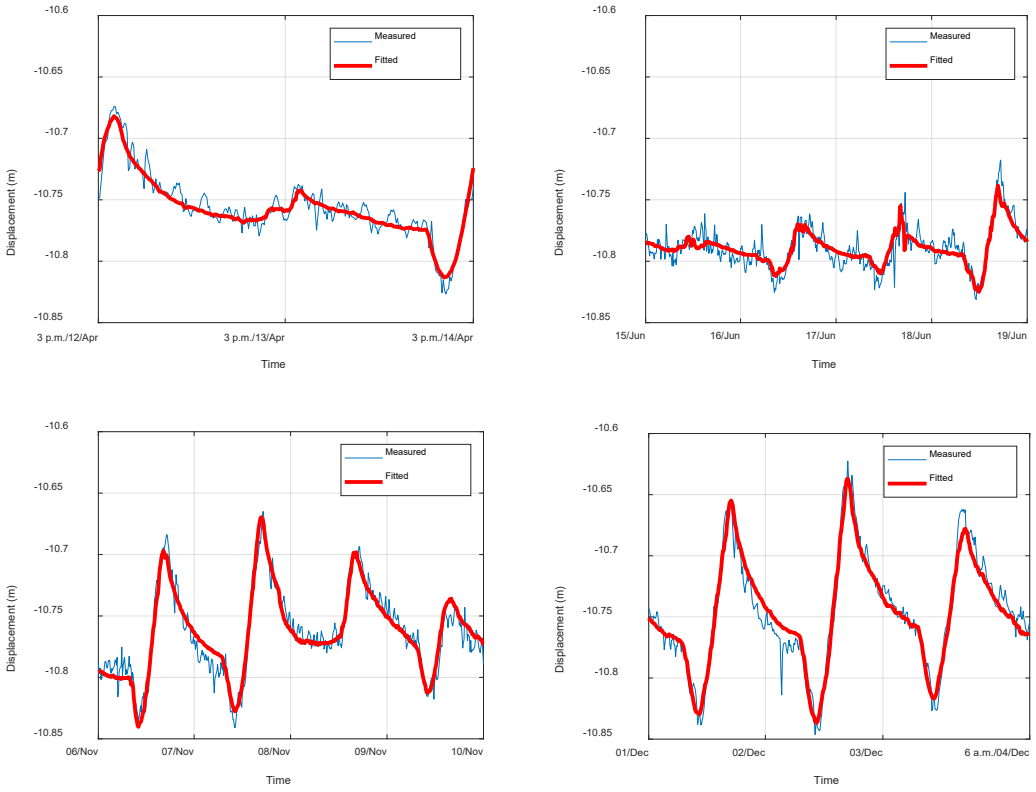

(a) East-west direction

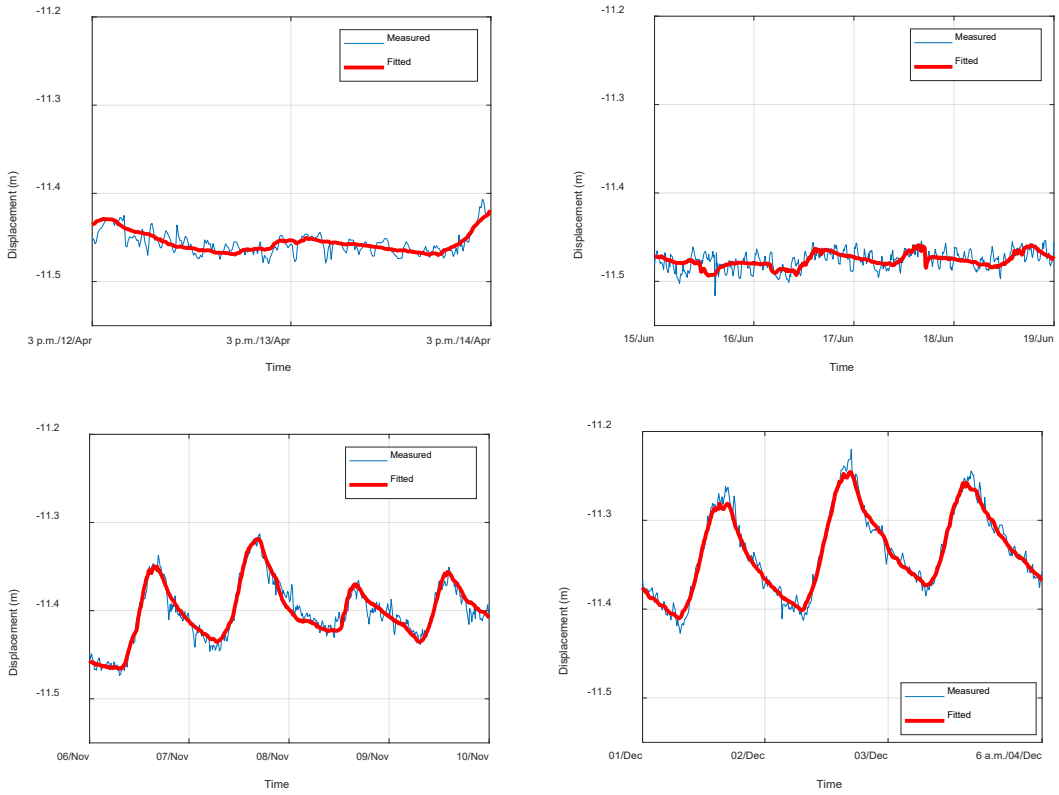

(b) North-south direction

Figure 8. The measured and fitted horizontal displacement of the tower top by RLR

Verification of the regression analysis

In order to assess the accuracy of the regression models, the models are applied to the other set of data for verification. A 72-hours dataset with light breeze is selected, which is from 00:00:01 on November 21 to 00:00:00 on November 24, 2013. Figure 9 compares the predicted results by the OLR and RLR models. The proposed RLR model predicts the tower displacement very well and the RMSE is 8.09 mm and 8.07 mm in the east-west and north-south directions, respectively. However, the OLR model predictions are biased in both directions and the RMSE is 15.08 mm and 9.92 mm. This demonstrates that the RLR model is more accurate and robust than the OLR model.

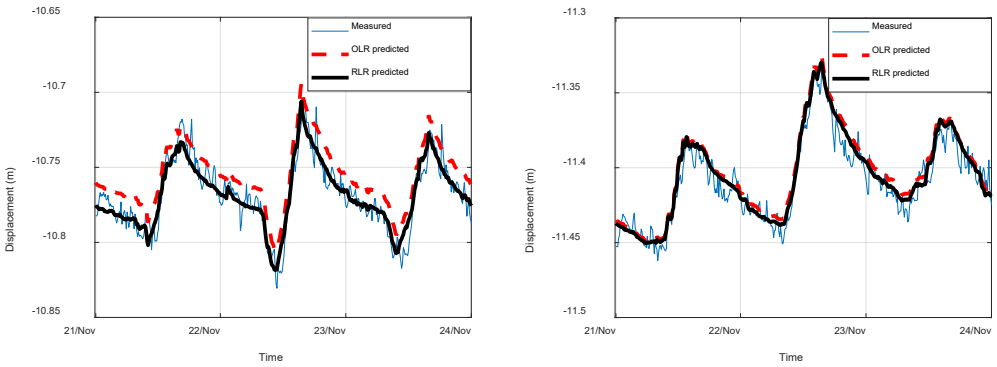

(a) East-west direction (b) North-south direction

Figure 9. Comparison of predicted results by OLR and RLR models

Responses during monsoon period

The Canton Tower is also subjected to wind loading. Separation of the wind- and temperature-induced responses is challenging in practice. The proposed regularized regress model is able to predict the temperature-induced displacement and will be applied to the monsoon period with relatively large wind. The difference between the total displacement and the predicted temperature displacement can then be regarded as the pure wind-induced one. Figure 10 shows the wind speed and wind direction from 00:00:01 on December 18 to 00:00:00 on December 21. The sampling rate is 0.2 Hz. The wind direction measures clockwise from the north. The wind direction varies rapidly in most of time.

The proposed RLR model is applied to the measured temperature data and displacement during the period. The measured and predicted displacement in the east-west direction is shown in Figure 11. As described above, the predicted structural displacement is induced by the temperature loading solely. The difference of the two

sets of displacement is due to the wind load. The raw wind speed data is decomposed into two perpendicular directions and the east-west component is

$$u = -u_0 \times \sin(\theta) \tag{13}$$

where u_0 is the measured wind speed, θ is the measured wind direction, and the negative sign is used such that the wind speed is positive to the east, same as the displacement. The wind-induced east-west displacement is plotted in Figure 12 together with the wind speed in the east-west direction, in which the data are averaged over 10 minutes to remove the dynamic component. It shows that the wind-induced displacement is basically in correlation with the wind speed, that is, the high wind speed contributes to the large displacement and low speed corresponds to small displacement. The occasional inconsistency may be caused by the GPS measurement noise.

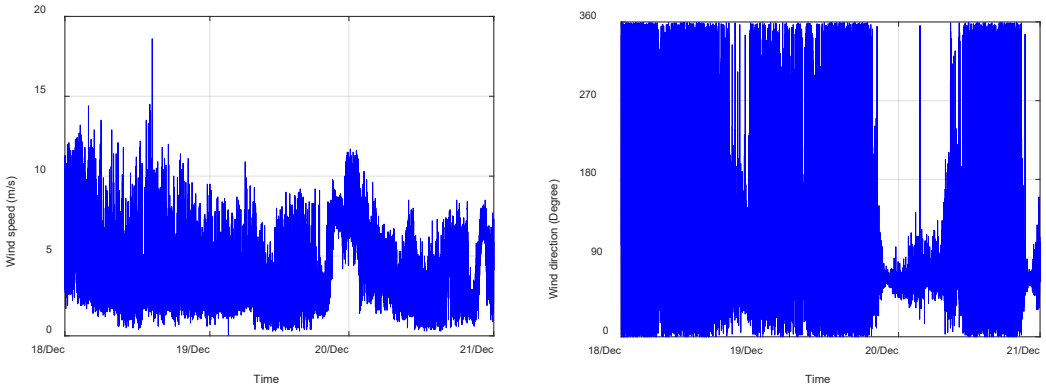

(a) Wind speed (b) Wind direction

Figure 10. Wind speed and direction on Dec. 18-20, 2013

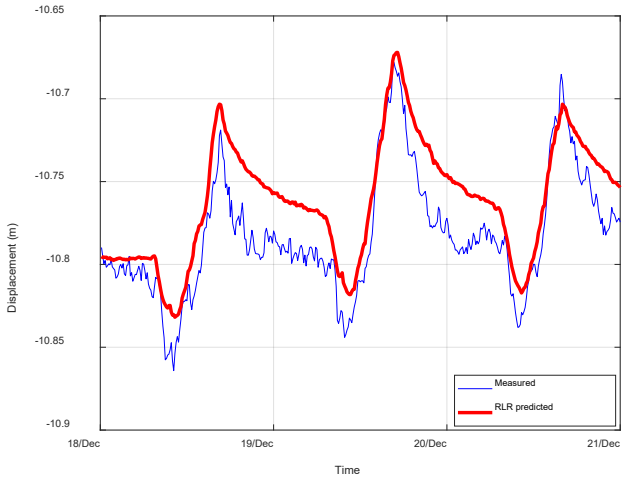

Figure 11. Measured and predicted east-west displacement during wind

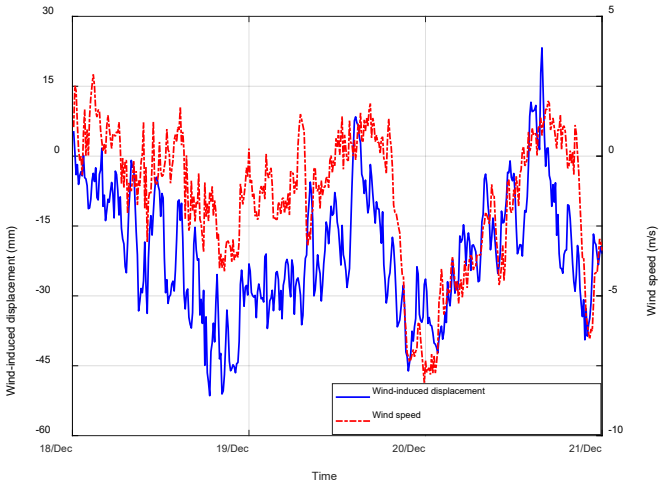

Figure 12. Wind speed and wind-induced displacement in east-west direction

Conclusions

In this article, the multiple linear regression and regularization technique are employed to investigate temperature-induced displacement of the Canton Tower. As temperature data at different measurement points may be of high correlation, the ordinary linear regression (OLR) model, although fits the measurement data very well, fails to interpret the physical meaning of the model. This article proposes a method based on regression coefficients to describe the physical meaning of structures by

using the regularized linear regression (RLR) model. The results show that the coefficients of the model are consistent with the physical structure. This case study is a good example showing that using data-driven approaches should be of discretion and understand the physical problem well.

Acknowledgement

This research was supported by the Research Grants Council of the Hong Kong Special Administrative Region, China (Project No. PolyU 152621/16E) and NSFC Joint Research Fund for Overseas and Hong Kong and Macao Scholars (Project No. 51629801).

References

Breuer P, Chmielewski T, Gorski P, et al. (2008) The Stuttgart TV tower-displacement of the top caused by the effects of sun and wind. *Engineering Structures* 30(10):2771–2781.

Breuer P (2010) Monitoring the horizontal displacement of slim high towers caused by daily temperature variation and wind impact by application of static and kinematic GPS-mode: some results. In: *Proceedings of the 5th World Conference on Structural Control and Monitoring*, Tokyo, Japan, 12 - 14 July.

Brownjohn JMW (2005) Long-term monitoring of dynamic response of a tall building for performance evaluation and loading characterisation. In: *Proceedings of the 1st International Operational Modal Analysis Conference*, Copenhagen, Denmark, 26-27 April.

Brownjohn JMW and Pan TC (2008) Identifying loading and response mechanisms from ten years of performance monitoring of a tall building. *Journal of Performance of Constructed Facilities* 22(1): 24-34.

Chan WS and Xu YL (2008) *Establishment of Bridge Rating System for Tsing Ma Bridge: Statistical Modelling and Simulation of Predominating Wind Loading Effects*. Report No 3. Hong Kong: Department of Civil and Structural Engineering, The Hong Kong Polytechnic University.

Chen XZ, Su YX and Li D (2012) Study on the cooling effects of urban parks on surrounding environments using Landsat TM data: a case study in Guangzhou, southern China. *International Journal of Remote Sensing* 33:18, 5889-5914.

473 Hansen PC and O'Leary DP (1993) The use of the L-curve in the regularization of
474 discrete ill-posed problems. *SIAM Journal on Scientific Computing*
475 14(6):1487-1503.
476 Hastie T Tibshirani R and Friedman J (2009) *The Elements of Statistical Learning:*
477 *Data Mining, Inference, and Prediction (Second Edition)*. New York: Springer.
478 Hu Y, Liang GH, Li QB, et al. (2017) A monitoring-mining-modeling system and its
479 application to the temperature status of the Xiluodu arch dam. *Advances in*
480 *Structural Engineering* 20(2): 235–244.
481 Nayeri RD, Masri SF, Ghanem RG, et al. (2008) A novel approach for the structural
482 identification and monitoring of a full-scale 17-story building based on ambient
483 vibration measurements. *Smart Materials and Structures* 17(2):1-19.
484 Ni YQ, Xia Y, Liao WY, et al. (2009) Technology innovation in developing the
485 structural health monitoring system for Guangzhou New TV Tower. *Structural*
486 *Control and Health Monitoring* 16(1):73-98.
487 Ni YQ, Zhang P, Ye XW, et al. (2011) Modeling of temperature distribution in a
488 reinforced concrete supertall structure based on structural health monitoring data.
489 *Computers and Concrete* 8(3):293-309.
490 Peeters B, Maeck J and De Roeck G. (2001) Vibration-based damage detection in
491 civil engineering: excitation sources and temperature effects. *Smart Materials*
492 *and Structures* 10(3):518–527.
493 Pehlivan H, Aydin Ö, Gülal E, et al. (2015) Determining the behaviour of high-rise
494 structures with geodetic hybrid sensors. *Geomatics, Natural Hazards and Risk*

6(8):702-717.

Pirner M and Fischer O (1999) Long-time observation of wind and temperature effects on TV towers. *Journal of Wind Engineering and Industrial Aerodynamics* 79(1-2):1–9.

Seco A, Tirapu F, Ramirez F, et al. (2007) Assessing building displacement with GPS. *Building and Environment* 42(1):393-399.

Smith BS and Coull A (1991) *Tall building structures: analysis and design*. New York: Wiley.

Su JZ, Xia Y, Ni YQ, et al. (2017a) Field monitoring and numerical simulation of the thermal actions of a supertall structure. *Structural Control and Health Monitoring* 24 (4):e1900.

Su JZ, Xia Y, Zhu LD, et al. (2017b) Typhoon-induced and temperature-induced quasi-static responses of a supertall structure. *Engineering Structures* 143:91-100.

Tamura Y, Matsui M, Pagnini LC, et al. (2002) Measurement of wind-induced response of buildings using RTK-GPS. *Journal of Wind Engineering and Industrial Aerodynamics* 90(12-15):1783-1793.

Tian Y, Zhang N and Xia H (2017) Temperature effect on service performance of high-speed railway concrete bridges. *Advances in Structural Engineering* 20(6): 865–883.

Xia Q, Cheng YY, Zhang J, et al. (2017) In-Service Condition Assessment of a Long-Span Suspension Bridge Using Temperature-Induced Strain Data. *J.*

Bridge Eng., 22(3): 04016124.

Xia Y, Chen B, Weng S, et al. (2012) Temperature effect on vibration properties of civil structures, a literature review and case studies. *Journal of Civil Structural Health Monitoring* 2(1):29-46.

Xia Y, Zhang P, Ni YQ, et al. (2014) Deformation monitoring of a super-tall structure using real-time strain data. *Engineering Structure* 67, 29-38.

Zhou GD, Yi TH, Chen B, et al. (2017) A generalized Pareto distribution–based extreme value model of thermal gradients in a long-span bridge combining parameter updating. *Advances in Structural Engineering* 20(2): 202–213.